Microphysical characteristics of a convective precipitation system observed on July 04, 2012, over Mt. Halla in South Korea

Hyeon-Joon Kim, Keun-Ok Lee, Cheol-Hwan You, Hiroshi Uyeda, Dong-In Lee

Atmospheric Research 222 (2019) 74–87

Contents lists available at ScienceDirect

Atmospheric Research

journal homepage: www.elsevier.com/locate/atmosres

Microphysical characteristics of a convective precipitation system observed on July 04, 2012, over Mt. Halla in South Korea

Hyeon-Joon Kim[a], Keun-Ok Lee[b], Cheol-Hwan You[c], Hiroshi Uyeda[d], Dong-In Lee[a,c,*]

[a] Department of Environmental Atmospheric Sciences, Pukyong National Univ., Busan, Republic of Korea
[b] Laboratoire d'Aerologie, Université de Toulouse, CNRS, UPS, Toulouse, France
[c] Atmospheric Environmental Research Institute, Pukyong National Univ., Busan, Republic of Korea
[d] Nagoya University, Nagoya, Japan

ARTICLE INFO

Keywords:
Drop size distribution
Disdrometer
Orographic precipitation
Moist environment

ABSTRACT

During the 2012 Changma season of June and July, we conducted an intensive field observation to investigate the microphysical characteristics of orographic precipitation that passed around Mt. Halla (oriented west–east; height: 1950 m; width: 78 km; length: 35 km) in South Korea's Jeju Island. On July 04, 2012, Jeju Island experienced a convective precipitation system that developed in the southern part of a stationary front. With the goal of understanding the microphysical process of this system (precipitation intensity: 70 mm h^{-1}), we collected detailed data using 7 Parsivel disdrometers, a ground-based dual S-band Doppler radar, and GPS sounding. The convective precipitation developed in a considerably warm and moist environment (near-surface relative humidity: 94%) with dominant southwesterly winds of 4.7 m s^{-1} at low altitudes. The convective region was formed by a combination of coastal ascending air and considerably warm and moist low-level marine inflow. The coastal warm and moist ascending air activates the warm rain process of moisture uptaken from sea surface, increasing the concentration of large-sized raindrops (diameter: ≥ 5 mm). The continuous development of a convective region extending from the foothill to the upslope highlights that the convective updrafts continuously supply low-level moisture to the convective region. This influx of moisture and the condensation of small-, middle-, and large-sized raindrops combine to create a significant concentration of large-sized raindrops along the upslope of the mountain. Around the mountaintop, the fall of precipitation drives the breakup process aided by convective ascending airs, increasing the concentrations of small-sized raindrops. On the leeward side, the existence of orographically generated stationary wind convergences is notable. As a result and the marine inflow along the southeastern gentle slope, i.e., the convective region, continues to develop, thereby activating cold rain processes. This study sheds light on the variety of raindrop size distributions and moisture processes at locations relative to a single-peak mountain leading to localized heavy precipitation during the passage of an isolated convective precipitation event.

1. Introduction

Heavy precipitation systems are frequently observed in East Asia during the rainy season, which is called “Changma” in Korea, “Baiu” in Japan, and “‘Meiyu” in China. The Changma/Baiu/Meiyu season is characterized by considerably warm and moist environments with southwesterly winds prevailing at low altitudes. These winds persist from June to mid-July. The season is also characterized by significant precipitation that causes damage to human life and property through landslides and flash floods.

The complex topography of East Asia has been investigated by many previous studies (Jiang, 2003; Lin et al., 2001; Massmann et al., 2017) as one of the key factors linked to the intensification of precipitation systems [e.g., mesoscale convective systems (MCSs), typhoons, and isolated convective systems). When a precipitation system passes through the vicinity of the coastal mountainous regions, large amounts of water vapor from the warm sea surface are subjected to orographic lifting and/or blocking; the precipitation system may then trigger and/or modify cloud and precipitation systems (Rosenfeld and Ulbrich, 2003; Lee et al., 2014). The moist air advected to the mountain slope from the sea surface can grow to form small raindrops because of upslope condensation and the interaction of microphysical and dynamical processes, e.g., saturation of ascended moist air to above the lifted condensation level (LCL) by topography.

* Corresponding author at: Department of Environmental Atmospheric Sciences, Pukyong National Univ., Busan, Republic of Korea.
E-mail address: leedi@pknu.ac.kr (D.-I. Lee).

https://doi.org/10.1016/j.atmosres.2019.02.011
Received 20 June 2018; Received in revised form 15 February 2019; Accepted 20 February 2019
Available online 22 February 2019

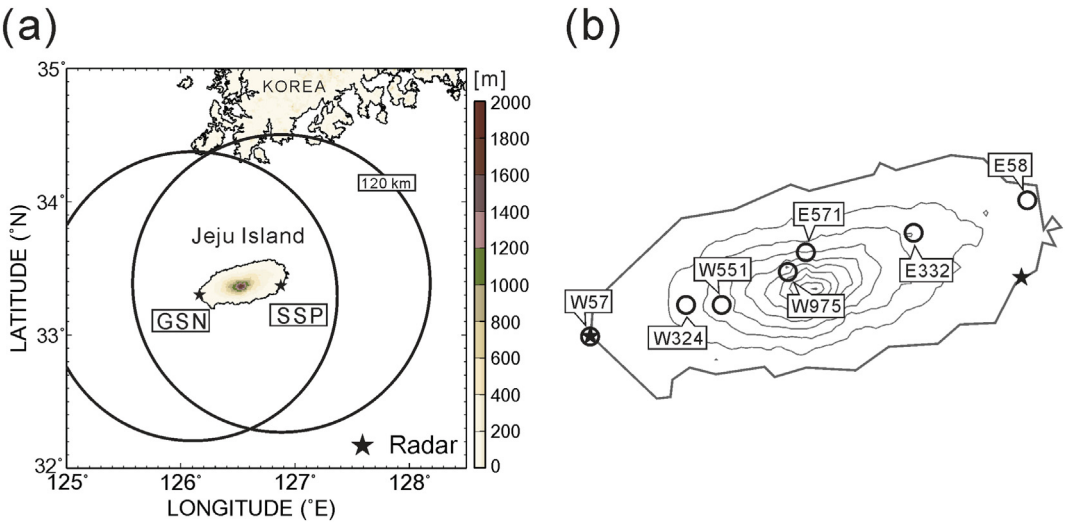

Fig. 1. (a) Elevation map of Jeju Island and observational ranges (120 km; circles) of the GSN and SSP radars. (b) Locations (black open circles) of the 7 Parsivel sites. The locations of GSN and SSP are indicated by stars. The topography is depicted by contours every 200 m.

Zwiebel et al. (2016) studied the microphysical processes occurring in precipitation systems developed along the complex topography of the southeastern part of France (top height: 1700 m) and the moisture supply from the warm Mediterranean Sea surface at low troposphere using in situ measurement instruments, such as disdrometers, X-band radars, micro-rain radars. They found that while the convective system passed over the complex topography, large liquid water content (LWC) and large-sized raindrops were formed owing to the coalescence effect of low-level clouds or fog over the mountain upslope. Their results demonstrate that the DSD is the fundamental result of the microphysical and dynamical processes.

The microphysical processes of precipitation systems have been studied at various mountainous regions in East Asia, such as the Central Mountain Range (CMR) of Taiwan and Mt. Halla at South Korea's Jeju Island. In the moist environment of the Meiyu season, a widespread stratiform region embedded in the precipitation system passed over the windward side of CMR (oriented southwest–northeast; height: 4 km; width: 120 km; length: 320 km). The precipitation amount of the stratiform region was greatly enhanced by terrain-induced local wind convergences at low altitudes (Feng and Chen Wang, 2011). Feng and Chen Wang (2011) found that many small hydrometeors falling from the convective region of the precipitation system were transported to the stratiform region because of orographically induced local wind convergence. Through the recycling of small-drop hydrometeors, microphysical interactions, such as collision and coalescence processes, in the convective region were activated between raindrops and small condensed droplets. This increased the concentration of raindrops supplied from the convective region in the stratiform region of the precipitation system.

Similar to the CMR of Taiwan, the warm and moist environment around Jeju Island of South Korea, an isolated elliptically shaped terrain with a relatively small horizontal scale (oriented in west–east direction; height: 1950 m; width: 35 km; length: 78 km), is well organized at low altitudes during the Changma season.

Despite the relatively small horizontal scale of the terrain, orographically induced intense precipitation systems are frequently observed in the vicinity of the Jeju Island terrain (Lee et al., 2010, 2012, 2014). There exist several southwesterly wind regimes depending on the wind speed: 1) the very-weak wind regime ($Fr \leq 0.2$): flow blocking by the steep isolated mountain on the island, which induces separation generating local convergence on the terrrain's leeward side, 2) the moderate wind regime ($0.2 < Fr \leq 0.5$): the co-existence of flow blocking and flow blowing over the mountain generates weak descending air on the leeward side, and 3) the strong wind regime ($0.5 < Fr$): strong ascending air is present on the windward side and dry descending air on the leeward side. Using numerical simulations with a cloud-resolving model (CRM), Lee et al. (2014) investigated the microphysical structures associated with the convective region of precipitation that is developed in the environment with low-level southwesterly winds being $\leq 5\ m\ s^{-1}$. They found that southwesterlies in low altitudes deliver abundant water vapor from the warm sea surface into the convective region around the lateral side of the terrain. The water vapor is then lifted owing to orographically generated convergence. Thus, microphysical processes, including the condensation of vapor to cloud water, and processes of collection and coalescence of raindrops are activated. Their study addressed the microphysical characteristics within the convective systems passing over the mountainous region of Jeju Island using fine-scale numerical simulations with CRM. Further detailed studies based on measurement data are required to improve the understanding of the microphysical analysis of orographically enhanced precipitation systems.

To investigate the microphysical characteristics of orographically enhanced precipitation systems around Mt. Halla at Jeju Island, the Group of Environmental Atmospheric Research of Pukyong National University (GEAR-PKNU) conducted an intensive observation period (IOP) at Jeju Island during the Changma season from June 25, 2012 to July 15, 2012. During the IOP, 7 Parsivel disdrometers were installed along the mountainous range of Jeju Island at altitudes ranging from 57 to 975 km above sea level (ASL; see Fig. 1 for locations). We also installed 13 rain gauges, 1 automatic weather system, and 64 GPS soundings. To collect three-dimensional (3D) data of reflectivity and wind, we used 2 operational S-band Doppler radar systems installed in the west and east of Jeju Island by the Korean Meteorological Administration (KMA). During the IOP, 6 heavy precipitation events associated with the Changma front passed over Jeju Island with various locations relative to the mountain peak. From these events, we selected and isolated a convective precipitation system that passed over the 7 Parsivel sites along the long axis of Mt. Halla (from west to east) on July 04, 2012. We investigate the DSD characteristics of the orographically enhanced convective system in the warm and moist environment in the very-weak wind regime ($Fr \leq 0.2$ with a low-level southwesterly wind $\leq 5\ m\ s^{-1}$), a similar environment to that of Lee et al. (2012, 2014), using the measurement dataset obtained from the intensive field campaign. The contents of this paper are organized as follows. In Section 2, we present our analysis of data and methods. In Sections 3 and 4, radar reflectivity and 3D wind distribution from 2 Doppler radars and DSD

analysis on each Parsivel site are presented, respectively. In Section 5, we discuss and summarize the study.

2. Observational data and methodology

2.1. Intensive field campaign

2.1.1. IOP measurement dataset

The intensive field campaign occurred during the IOP from June 25, 2012 to July 15, 2012 at Jeju Island, South Korea. During the IOP, 7 identical Parsivel disdrometers (hereafter simply called "Parsivel") were installed along the long axis (southwest to northeast) of Mt. Halla across Jeju Island (open circles in Fig. 1b). This device is a laser-optical disdrometer with an optical sensor and a laser diode that can classify the type of precipitation (drizzle, drizzle/rain, rain, mixed rain/snow, snow, snow grains, sleet, and hail) (Löffler-Mang and Joss, 2000). The device can detect the diameter of raindrops in the range 0.2–25 mm and the fall velocity of the raindrop in the range 0.2–20 m s^{-1} with a fine temporal resolution of 1 min. For better understanding, the 7 Parsivels were named according to their location relative to the mountaintop with an alphabet (W for west; E for east), and the altitude information was denoted by a number (unit: m); e.g., W975 indicates the Parsivel installed on the western slope of the mountain at a height of 975 m ASL. We installed 4 Parsivels on the western slope, namely W57, W324, W551, and W975, and 3 Parsivels on the eastern slope, namely E56, E332, and E571.

The 64 GPS soundings were launched every 12 h during the IOP at the GSN radar site (Fig. 1). Based on the sounding measurement, we were able to calculate several environmental parameters, including LCL (m), relative humidity (RH, %), temperature (°C), dew-point temperature (°C), water vapor mixing ratio (g kg^{-1}), Froude number (*Fr*) below the mountaintop, and average wind speed and wind direction between near-surface and 2 km ASL.

2.1.2. Calculation of DSD parameters

To retrieve meteorological parameters, non-meteorological data (e.g., insect, leaf) were removed using a fall velocity-based filter proposed by Kruger and Krajewski (2002), which is expressed in Eq. (1):

$$|V_{measured} - V_{ideal}| < C \times V_{ideal} \tag{1}$$

where $V_{measured}$ (m s^{-1}) is the observed fall velocity, C is 0.6 (Jaffrain and Berne, 2010), and V_{ideal} (m s^{-1}) is the empirical fall velocity proposed by Atlas et al. (1973), as shown in Eq. (2):

$$V_{ideal}(\mathrm{D}) = 9.65 - 10.3\exp(-6D) \tag{2}$$

where D is the drop diameter.

For analysis, the DSD parameters of $N(D)$, N_0, D, μ, Λ, and LWC were calculated, where $N(D)$ is the number of drops per unit volume in unit size interval ($m^{-3}\,mm^{-1}$), N_0 is the intercept parameter ($m^{-3}\,mm^{-1-\mu}$), μ is the shape parameter, and Λ is the slope parameter (mm^{-1}). A three-parameter gamma distribution form [Eq. (3)] suggested by Ulbrich (1983) was used in the analysis:

$$N(D) = N_0 D^{\mu}\exp(-\Lambda D) \tag{3}$$

A truncated moments method (Vivekanandan et al., 2003) was used to calculate the accurate μ value, as described in Eq. (4). Here, γ represents an incomplete gamma function.

$$<D^n> = \int_{D_{min}}^{D_{max}} D^n N(D)dD = N_0\Lambda^{-(\mu+n+1)}[\gamma(\mu+n+1,\Lambda D_{max}) - \gamma(\mu+n+1,\Lambda D_{min})] \tag{4}$$

$$\eta = \frac{[\gamma(\mu+5,\Lambda D_{max}) - \gamma(\mu+5,\Lambda D_{min})]^2}{\gamma(\mu+3,\Lambda D_{max})\gamma(\mu+7,\Lambda D_{max}) - \gamma(\mu+3,\Lambda D_{min})\gamma(\mu+7,\Lambda D_{min})} \tag{5}$$

Eq. (5) is iterated until the η value between the complete and incomplete gamma functions is smaller than 0.001. η (Eq. (6)) calculated with the complete gamma function is used as the initial η. Then, the necessary Λ values are obtained when the difference between the initial and the calculated η values become smaller than 0.001 in Eq. (7):

$$\eta\ (\textit{calculated with gamma function}) = \frac{\left(\int_{D_{min}}^{D_{max}} N(D)D^4dD\right)^2}{\left(\int_{D_{min}}^{D_{max}} N(D)D^2dD\right)\times\left(\int_{D_{min}}^{D_{max}} N(D)D^6dD\right)} \tag{6}$$

$$\Lambda = \left(\frac{<D^2>[\gamma(\mu+5,\Lambda D_{max}) - \gamma(\mu+5,\Lambda D_{min})]}{<D^4>[\gamma(\mu+3,\Lambda D_{max}) - \gamma(\mu+3,\Lambda D_{min})]}\right)^{1/2} \tag{7}$$

In the gamma distribution, a large (small) Λ value tends to exhibit a more (less) steep DSD pattern. When the μ value is positive (negative), the shape of distribution is concave upward (downward). The median diameter D_0 is obtained using μ and Λ, as described in Eq. (8):

$$D_0 = \left(\frac{3.67+\mu}{\Lambda}\right) \tag{8}$$

The total number concentration N_T was calculated in Eq. (9):

$$N_T = \int_0^{\infty} N(D)dD \tag{9}$$

The LWC was calculated in Eq. (10), where ρ_w is the water density (kg m^{-3}):

$$\mathrm{LWC} = \frac{\pi\rho_w}{6}\int_0^{\infty} N(D)D^3dD \tag{10}$$

The radar reflectivity was calculated in Eq. (11):

$$\mathrm{Z} = \int_0^{\infty} N(D)D^6dD \tag{11}$$

In this study, three diameter categories of raindrops were defined: 1) small: diameter (D) < 1 mm; 2) middle: 1 mm ≤ D < 3 mm; and 3) large: D ≤ 3 mm. The values 0.5, 1.8, and 3.7 mm were used as the representative diameters of the small, middle, and large diameter categories, respectively.

2.2. Operational data

The 3D fields of reflectivity and Doppler velocity were obtained using dual S-band Doppler radars operated by the KMA, one at GSN (Gosan) and the other at SSP (Seongsan) (denoted using star marks in Fig. 1). The dual Doppler radars covered 250 km each, and together, they covered the entire Jeju Island every 10 min. The 2 Doppler radars of GSN and SSP have identical specifications with sampling resolutions of 500 m in the radial direction and 1.0° in the azimuthal direction. Each volume scan includes observations at 15 elevation angles (0.5°, 0.6°, 0.8°, 1.0°, 1.5°, 2.0°, 2.5°, 3.5°, 4.5°, 6.0°, 7.8°, 10.5°, 13.7°, 18.1°, and 24.0°). A mosaic of the two radii was created to reduce the beam blockage caused by topography.

Dual S-band Doppler radar data of the spherical coordinate system are interpolated into a Cartesian coordinate system with vertical and horizontal grid intervals of 250 m and 1 km. A Cressman-type weighting function (Cressman, 1959) is used for interpolation with fixed horizontal (1.5 km) and vertical (1.0 km) effective radii of influence. In the region where the 2 radars overlap, a larger reflectivity value was selected. Using the interpolated 3D reflectivity data, the characteristics of the vertical reflectivity profile in the low-level southwesterly wind environment were investigated according to the contoured frequency via altitude diagram (CFAD; Yuter and Houze Jr, 1995) analyses within the three analysis domains (windward, mountaintop, and leeward) of Jeju Island. CFAD analyses of the reflectivity were conducted every 1 dBZ in the range of 5–60 dBZ from 2100 LST to 2220 LST on July 04, 2012. To retrieve the 3D wind (u, v, and w) field, a variational method proposed by Liou and Chang (2009) was employed. Detailed analysis

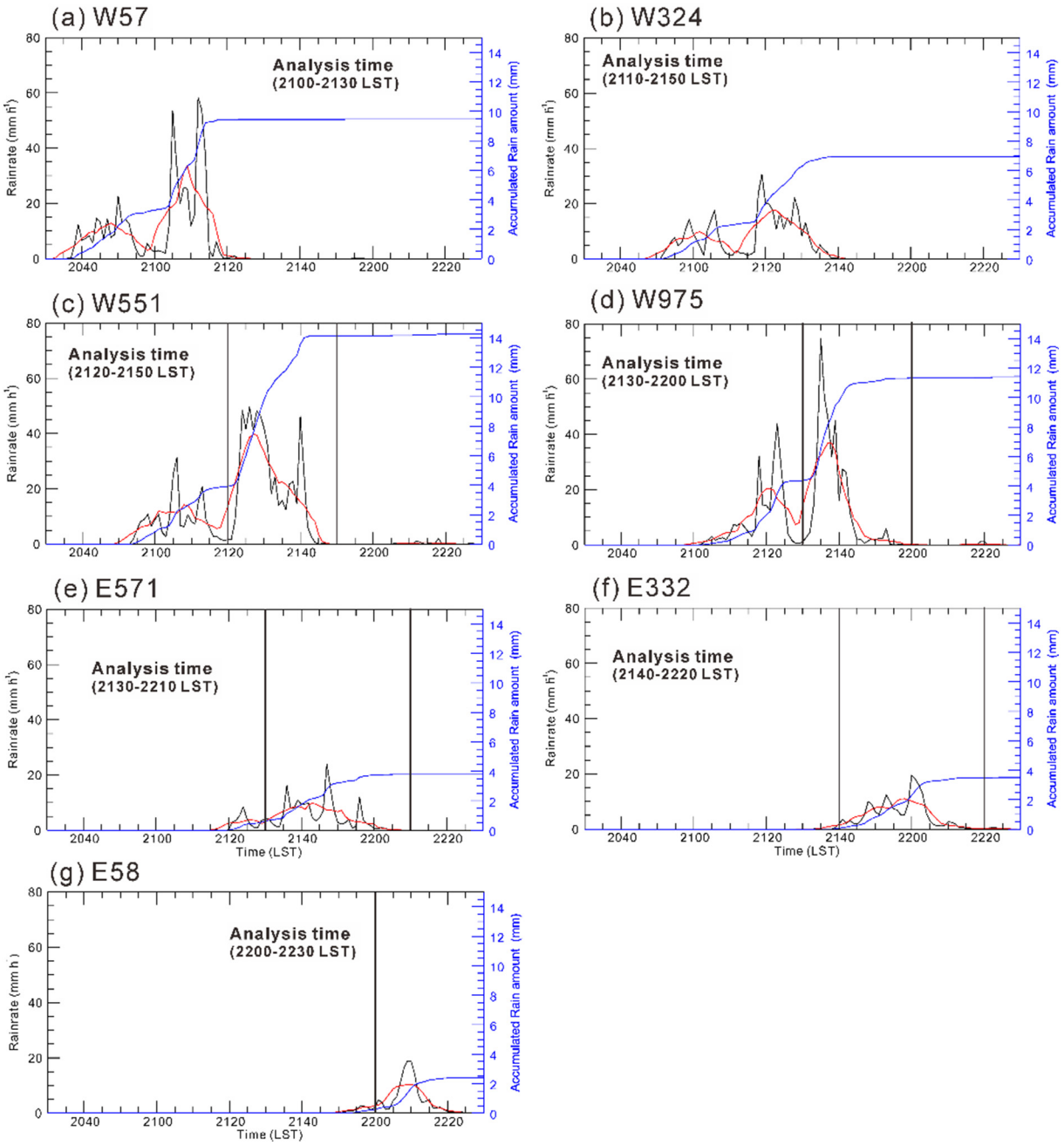

Fig. 2. Rainfall intensity every 1 min (black line, mm h^{-1}), averaged rainfall intensity every 5 min (red line, mm h^{-1}), accumulated rain amount (blue line, mm), and analysis period (boxes) at (a) W57, (b) W324, (c) W551, (d) W975, (e) E571, (f) E332, and (g) E58. (For interpretation of the references to colour in this figure legend, the reader is referred to the web version of this article.)

results of 3D reflectivity and wind distributions are provided in section 3.

To focus on the convective region, we chose a region with reflectivity values higher than 38 dBZ (Gamache and Houze Jr, 1982) at 2 km ASL and without a bright band in the layer where air temperature is around 0 °C: in this study, ~4.2 km. In addition, the "analytical period" was decided based on the Parsivel rain rate. A period during which the rain rate continuously exceeded 10 mm h^{-1} was selected at each Parsivel site (Fig. 2). For example, the analysis period of site W57 was from 2100 UTC to 2130 UTC on July 04, 2012 (Fig. 2a); the averaged DSD parameters during that period are described in section 4.

To understand the synoptic environment, the mesoscale model (MSM) data with a temporal resolution of 3 h and a horizontal resolution of 5 km with 14 vertical levels operated by the Japan Meteorological Agency were used.

3. Overview

3.1. Synoptic environment

An east–west extended stationary front was situated over the southern part of Jeju Island. The southwesterly wind was dominant over Jeju Island due to the north pacific anticyclone located in the southeast of the Island at 1800 LST on July 04, 2012 (not shown). Table 1 lists the environmental parameters obtained from an upper-air sounding launched at the GSN radar site (for the location, see Fig. 1) at 0900 LST on July 04, 2012, about 9 h prior to the approach of the precipitation system. The LCL was ~100 m ASL, which is an altitude

Table 1
Environmental parameters obtained from upper-air sounding data at GSN at 0900 LST on July 04, 2012: average wind speed and RH (relative humidity) from the near surface to 2 km ASL, the near-surface temperature, *Fr*, *N* (the Brunt–Vaisala frequency), LCL (lifted condensation level), LFC (the level of free convection), and CAPE (the convective available potential energy).

Parameters	
Wind Speed	4.7 m s^{-1}
RH	94%
Surface temperature	21.7 °C
Fr	0.2
N	0.01
LCL	994.4 hPa (100 m ASL)
LFC	989 hPa (150 m ASL)
CAPE	0.6 J kg^{-1}

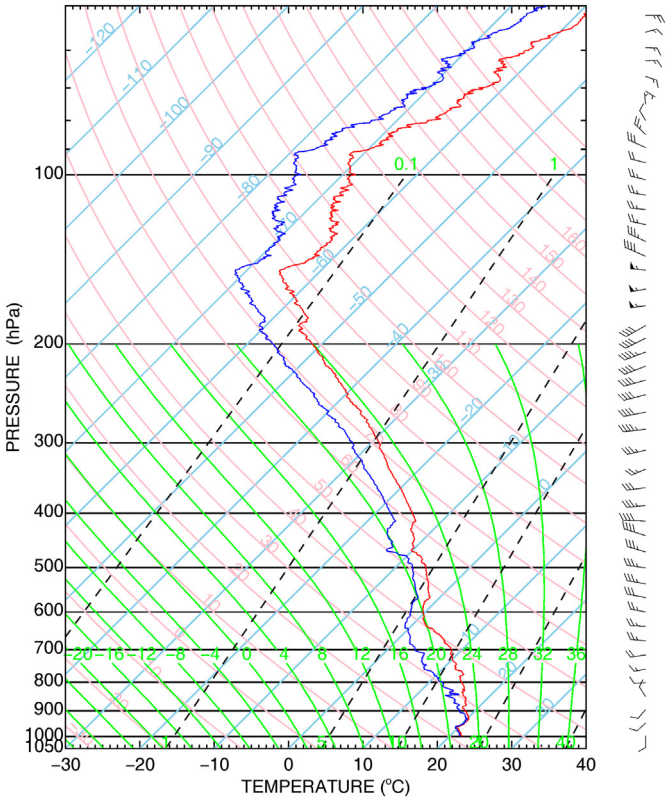

Fig. 3. Skew-T/log P diagram using the upper-air sounding data launched at GSN at 0900 LST on July 04, 2012. Red line show the environmental temperature (°C), blue line show the dew-point temperature (°C). (For interpretation of the references to colour in this figure legend, the reader is referred to the web version of this article.)

less than those of both the W324 and E332 sites (see Fig. 1b). The averaged RH value between the surface and 2 km ASL was as high as 94%. The *Fr* value was calculated to be ~0.2 with an average wind speed of 4.7 m s^{-1}, indicating that the moist air near the surface on the windward side of Mt. Halla likely detoured (Yoshizaki et al., 2000; Lee et al., 2012). This low *Fr* value indicates that the moist air at low altitudes goes around Mt. Halla (the very-weak wind regime, Lee et al., 2014). At 150 m ASL, the level of free convection (LFC) was low. In addition, the convective available potential energy (CAPE) was as low as 0.6 J kg^{-1} (Table 1). The low CAPE value is one of the environmental characteristics of the rainy season in East Asia (Riemann-Campe et al., 2009). At 0900 LST, a 0 °C level located at 4.2 km ASL (605 hPa) with near-saturated air mass is seen at altitudes between the surface and 1.5 km (840 hPa) and at altitudes between 4 and 6 km ASL

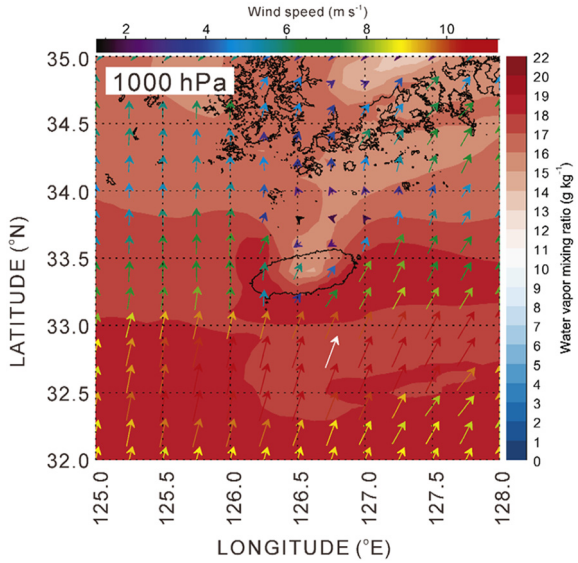

Fig. 4. Horizontal distribution of the water vapor mixing ratio (g kg^{-1}, shades) and wind (colored vectors) at the 1000-hPa level from MSM data at 1800 LST on July 04, 2012.

(625–480 hPa), where an RH of ≥85% is seen. The air condition at altitudes between 400 and 730 m ASL (960–920 hPa) was stable (Fig. 3). The average value of the water vapor mixing ratio (q) at altitudes between the surface and 1 km was as high as 15 g kg^{-1} (Fig. 3). At 1800 LST, large q values are continuously observed in the west, south, and east coastal regions of Jeju Island (Fig. 4), whereas relatively dry air masses with $q \leq 15$ (g kg^{-1}) are locally distributed at the north of the island in the environment with the low-level southwesterly wind.

3.2. Precipitation system on July 04, 2012

The horizontal reflectivity distribution at 2 km ASL and the time–height cross-section of the maximum reflectivity of the convection region (a solid lined box in Fig. 5) are displayed in Figs. 5 and 6, respectively. While the convective region passed over the mountain (from the western to the eastern coast), it continuously developed. In the time the precipitation system traveled from the western coast to the foothill of the terrain (2100 LST–2110 LST; Fig. 5a and 5b), the horizontal area of the convective region over the western foothill of the terrain from 5 to 21 km^2 at 2 km ASL grew. The height of maximum reflectivities exceeding 42 dBZ gradually increased to 6 km ASL (Fig. 6). At 2120 LST, the enhanced convective region observed continuously over the upslope of the mountain (Fig. 5c) and the vertical range of reflectivity stronger than 51 dBZ extended to altitudes lower than 2 km ASL (Fig. 6). Because the convective core did not pass over W324, the LWC values at W324 were lower than those at the adjacent W551.

During 2120 LST–2130 LST (Fig. 5c and 5d), the area near the mountaintop with a reflectivity of at least 42 dBZ enlarged sharply from 17 to 41 km^2. During 2140 LST–2150 LST (Fig. 5e and 5f), the convective region propagated to the eastern slope and the region with reflectivity stronger than 48 dBZ was continuously distributed from the above 0 °C level up to 5.5 km ASL (Fig. 6). Moreover, the heights corresponding to the reflectivity of at least 33 dBZ increased up to 8 km ASL or more. From 2100 LST to 2200 LST, while the convective region passed from the windward to the leeward side of the terrain, the maximum height at which reflectivity exceeded 33 dBZ gradually increased from 6 km to > 8 km ASL (Fig. 6). Post 2200 LST, the convective region passed over the eastern coast, reflectivities stronger than 42 dBZ were barely identified (6 km^2 at 2200 LST) (Fig. 5g and 5h), and the height at which reflectivities over 33 dBZ were measured decreased (Fig. 6). While our target convective cell was passing over Jeju Island,

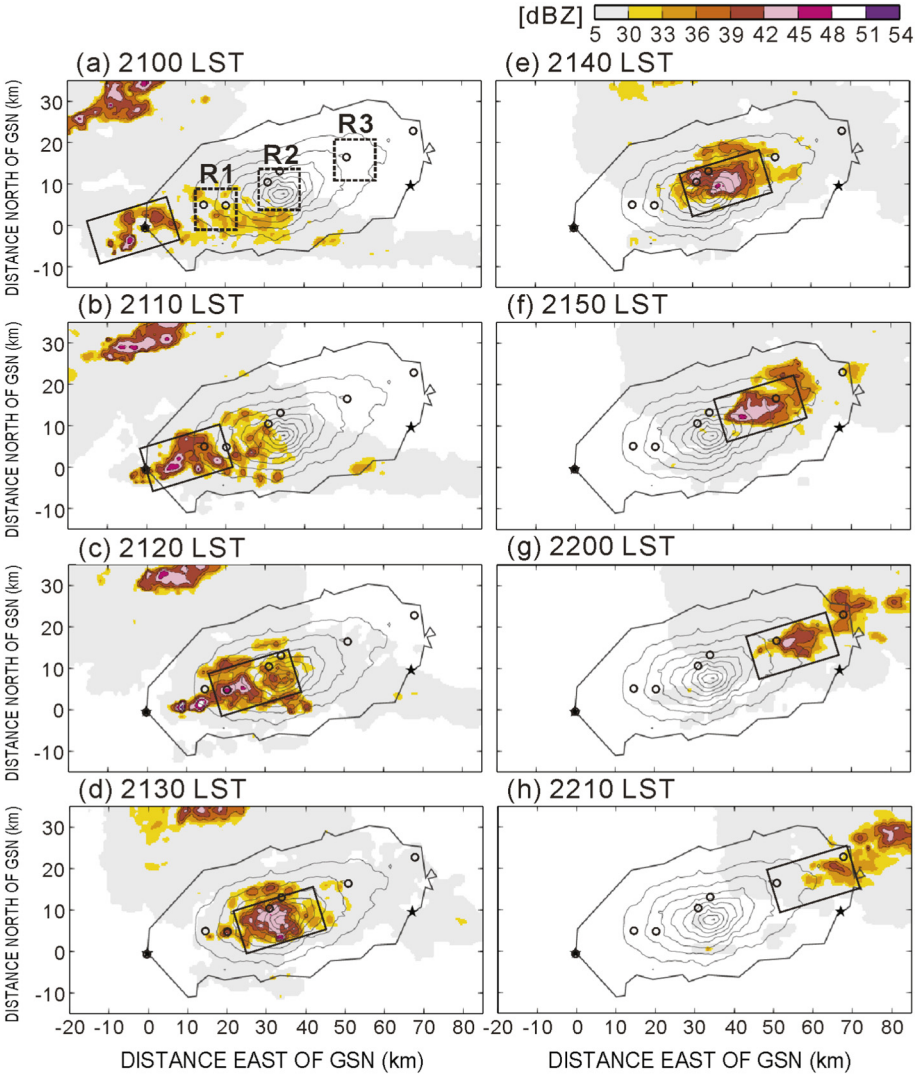

Fig. 5. Horizontal distributions of radar reflectivity at 2 km ASL at (a) 2100 LST, (b) 2110 LST, (c) 2120 LST, (d) 2130 LST, (e) 2140 LST, (f) 2150 LST, (g) 2200 LST, and (h) 2210 LST on July 04, 2012. The locations of the GSN and SSP radars are indicated by black stars on the western and eastern sides of Jeju Island. The locations of the Parsivel sites are indicated by open circles. The three rectangular areas (R1 (windward size), R2 (mountaintop), and R3 (leeward side)) in Fig. 5a indicate the horizontal area for the CFAD analysis (Fig. 7).

another convective system was situated to the north of Jeju Island, 20 km north of GSN (Fig. 5). These two convective systems are spatially close; however, the fine-resolution 3D wind field obtained by the two Doppler radars confirmed the independence of these systems.

Fig. 7 shows the CFAD during the passage of the convective precipitation system over the island's windward side (R1), the mountaintop (R2), and the leeward side (R3) (boxes in Fig. 5a). On the windward side (R1, Fig. 7a), strong reflectivity ranging from 30 dBZ to 40 dBZ was distributed from the surface upto 6 km (above the 0 °C level at 4.2 km) with a normalized frequency ≥ 60%. Conversely, a low frequency of < 20% is observed for weak reflectivities between 10 and 25 dBZ below 5 km ASL. These results demonstrate the active warm and cold rain microphysical processes on the windward side of the island. Near the mountaintop (Fig. 7b), the frequency of reflectivities ≤25 dBZ increased as compared to those of R1 (Fig. 7a), thus maintaining a large frequency (above 50%) for strong reflectivities ≥30% below 5 km ASL. On the leeward side (R3, Fig. 7c), the frequency of both the weak (10–20 dBZ) and moderate (20–30 dBZ) reflectivities were strong, exceeding 70%, from the surface to altitudes above the 0 °C level.

In addition, the maximum reflectivity on the leeward side at the surface was ~40 dBZ, whereas a higher reflectivity of ~50 dBZ was observed in the windward and mountaintop regions. The horizontal and vertical distributions of the vertical wind from 2100 LST to 2210 LST on July 4, 2012 are displayed in Figs. 8 and 9, respectively. For the vertical distribution, we used a cross-section line a − b, depicted in Fig. 8a. At 2100 LST, the convective region (contours in Fig. 8a) traveled over the western coastal region and ascending air with a velocity exceeding 2 m s^{-1} and was dominant over the western coast (Fig. 8a); this ascending air was distributed throughout low altitudes below 2 km ASL (~16 km from a; Fig. 9a). From 2110 LST to 2120 LST (Figs. 8b and 8c and 9b and 9c), while the convective region passed over the windward side, descending air stronger than 1.0 m s^{-1} was dominant at heights of 2–7 km ASL owing to strong precipitation within the convective region. Within the convective cell, convective updrafts of about 0.5 m s^{-1} were consistently found at low levels (not shown). When the convective region passed over the top part of a mountain at around 2130 LST (Figs. 8d and 9d), descending air of 2 m s^{-1} was consistently observed within the system below 6 km ASL (Fig. 6d). At 2140 LST, when the convective region was located near the top part of a mountain, ascending air stronger than 2 m s^{-1} was highlighted ahead of the convective region over the leeward side. It ranged from near the surface to 5 km ASL (Figs. 8e and 9e). Due to the strong ascending air, the maximum height of the reflectivity area with 36 dBZ was about 6 km ASL on the windward side but increased to over 7 km ASL on the leeward side

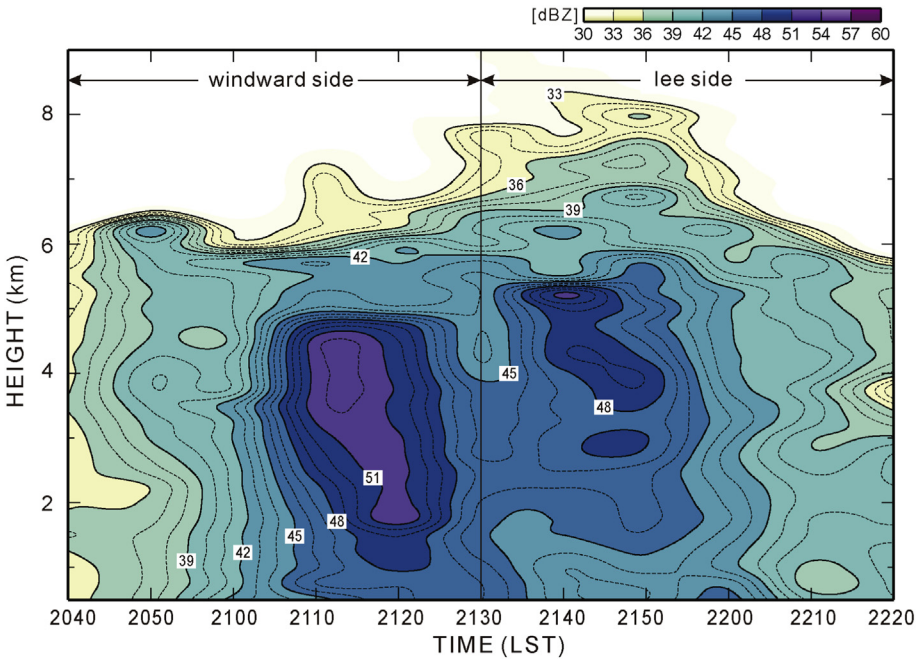

Fig. 6. Time–height cross section of the maximum reflectivity of the convective region (the solid lined box in Fig. 5) from 2040 LST to 2220 LST on July 04, 2012. Contours with dashed lines show the maximum reflectivity every 1 dBZ from 33 dBZ. Shading and contours with the solid lines indicate the maximum reflectivity every 3 dBZ from 33 dBZ.

(Fig. 6 and Fig. 9). The cloud top temperature decreased about −50 °C while the convective cell passed over the top of a mountain (not shown). From 2150 LST to 2200 LST, the convective region passed over the local ascending air ($> 1\,m\,s^{-1}$) existing at the leeward side and strong reflectivity was observed above 1 km ASL (Fig. 6). Post 2210 LST (Figs. 8h and 9h), strong reflectivity was barely identified as the convective region passed over the eastern coast.

4. DSD characteristics

4.1. Averaged DSD parameters

Figs. 10 and 11 show the averaged LWC ($g\,m^{-3}$), maximum reflectivity (dBZ) obtained from the 7 Parsivels, and averaged $N(D)$ ($m^{-3}\,mm^{-1}$) during the analytical period. Among all the sites, W57 exhibited the maximum reflectivity (53 dBZ) and highest LWC ($0.6\,g\,m^{-3}$), as shown in Fig. 10a, together with the highest concentration ($N(D)$) of large raindrops. The largest rain drop diameter (~6.5 mm) recorded was at W57 (light blue line in Fig. 11). The concentration $N(D)$ of large rain drops (3.2 mm) at W57, W551, and W975 was $> 10\,m^{-3}\,mm^{-1}$ (blue, gray, and black lines in Fig. 11). The maximum LWC value was $0.96\,g\,m^{-3}$; this value was observed at W551 (Fig. 10). In contrast, the highest concentration $N(D)$ of small raindrops was identified at W551 (gray line in Fig. 11). The same area, which is the windward slope including W551, exhibited reflectivities stronger than 30 dBZ at heights lower than 1 km ASL (Fig. 7a). The concentration $N(D)$ of middle-sized raindrops (D: ~1.8 mm) was relatively high along 3 sites on the western slope of the mountain, specifically 100, 200, and $150\,m^{-3}\,mm^{-1}$ at W324, W551, and W975, respectively (Fig. 11). Even though large raindrops contribute more toward strong reflectivity, the small to middle-sized raindrops also increase reflectivity (refer to Eq. (11)).

The LWC value on the leeward side, i.e., at sites E571, E332, and E58, was ~$0.3\,g\,m^{-3}$ (Fig. 10a). The values of maximum reflectivity at these sites were lower than those observed near the surface on the windward side, but the values still exceeded 40 dBZ (Fig. 10a). Furthermore, the lee-side sites (E571, E332, and E58) had relatively low values of $N(D)$, specifically $< 100\,m^{-3}\,mm^{-1}$ of middle- and large-sized raindrops ($1.5 < D \leq 4.5$ mm; Fig. 11). There was a large value of $N(D)$ for small raindrops at all 3 sites of the leeward side; the largest $N(D)$ value of ~$1000\,m^{-3}\,mm^{-1}$ for raindrops smaller than 0.5 mm was observed at E332 (orange line in Fig. 11). Meanwhile, the value of $N(D)$ for small raindrops was low ($\leq 600\,m^{-3}\,mm^{-1}$) at E58 (brown line in Fig. 11). The patterns of the relative difference in LWC for each site (windward side, mountaintop, and leeward side) is similar to the patterns of the accumulated rain amounts for each site (9.5 mm at W57, 6.9 mm at W324, 14.3 mm at W551, 11.4 mm at W975, 3.8 mm at E571, 3.5 mm at E332, and 2.4 mm at E58) (Fig. 2). Relatively greater rainfall amounts were observed on the windward side compared to those on the leeward side. Further, W324 had great concentration of small and middle-sized raindrops resulting in the highest amount of rainfall.

4.2. Variability of DSD parameters: N(D), D_0, and N_T

4.2.1. Windward side

We computed an average $N(D)$ value at 5-min intervals for W57, W324, W551, and W975 on the windward side of the terrain (Fig. 12). The time series of the DSD parameters D_0 and N_T at the 7 Parsivel sites are shown in Fig. 13. At the western coastal region (W57), as rainfall began, the $N(D)$ value of all raindrop diameters increased. For small raindrops, the $N(D)$ value increased from 271.5 to $511.9\,m^{-3}\,mm^{-1}$. For middle-sized raindrops, the value increased from 19.9 to $190\,m^{-3}\,mm^{-1}$. For large raindrops, the value increased from 1.4 to $4.0\,m^{-3}\,mm^{-1}$ (from red to orange lines in Fig. 12a). The increased $N(D)$ value was observed for the next 10 min (brown line in Fig. 12a), and it was observed that the diameter of the largest raindrops further increased to ~6 mm. During the next 5-min period (light green line in Fig. 12a), while the $N(D)$ of raindrops smaller than 0.6 mm was relatively constant around $500\,m^{-3}\,mm^{-1}$, the $N(D)$ of middle-sized and large-sized raindrops decreased from 131.7 to $14.9\,m^{-3}\,mm^{-1}$ and from 9 to $0\,m^{-3}\,mm^{-1}$, respectively. Later in the analytical period (green lines), the $N(D)$ decreased for all diameters. The large increase in raindrops of all diameters at W57 resulted in the largest D_0 value of 2.5 mm at 2112 LST (light blue line in Fig. 13a).

At site W324, the $N(D)$ of the middle- and large-sized raindrops greatly increased to 116.3 and $1.7\,m^{-3}\,mm^{-1}$, respectively, during the first 10 min of the analytical period (red and orange lines in Fig. 12b). Note that the value of $N(D)$ for small-sized raindrops was consistently high during the entire analysis period (Fig. 12b). N_T values over 1000

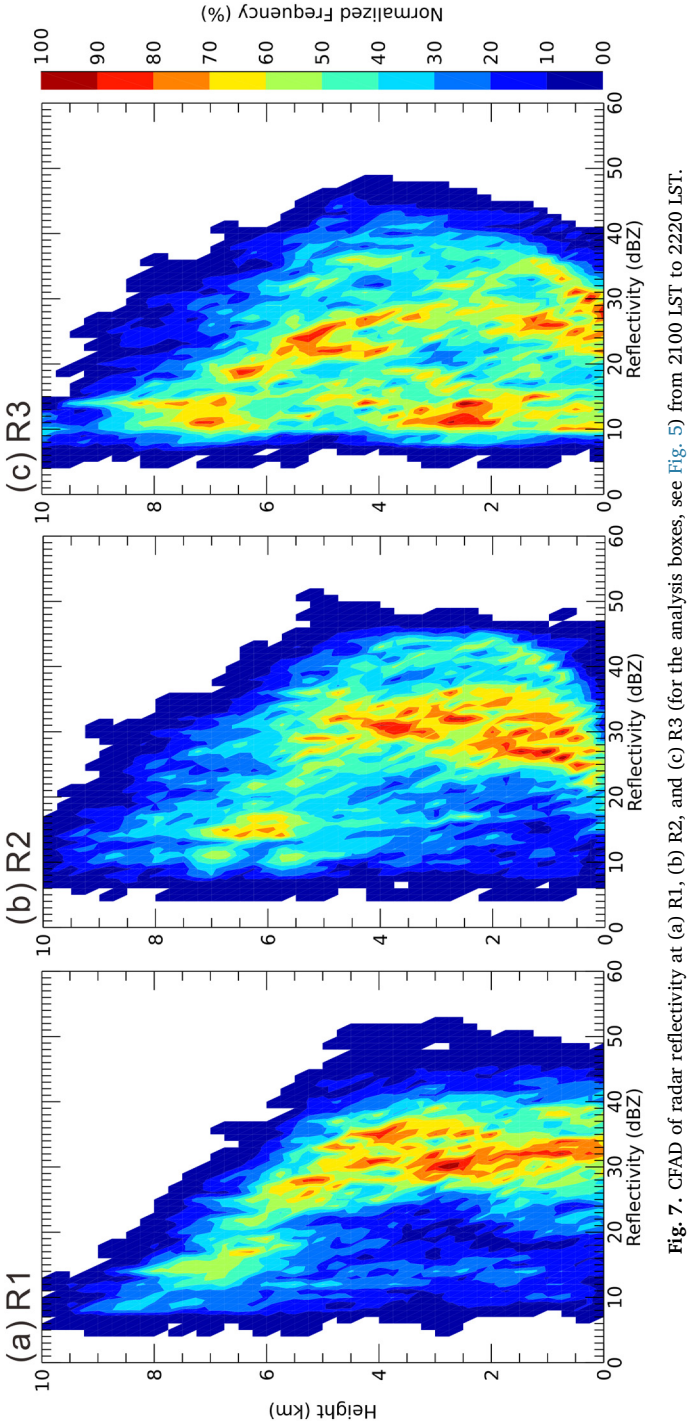

Fig. 7. CFAD of radar reflectivity at (a) R1, (b) R2, and (c) R3 (for the analysis boxes, see Fig. 5) from 2100 LST to 2220 LST.

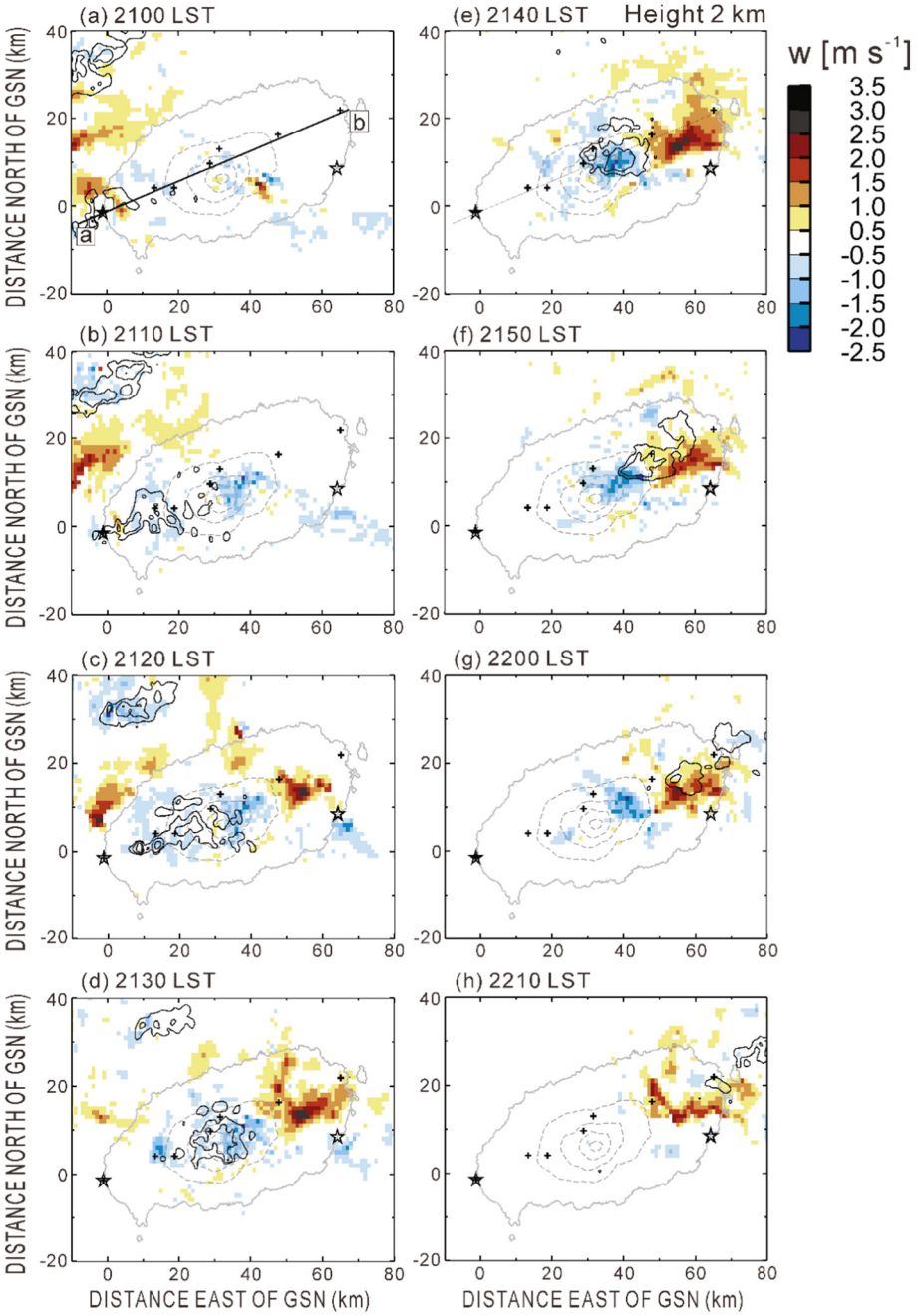

Fig. 8. Horizontal distribution of the vertical wind at 2 km ASL at (a) 2100 LST, (b) 2110 LST, (c) 2120 LST, (d) 2130 LST, (e) 2140 LST, (f) 2150 LST, (g) 2200 LST, and (h) 2210 LST on July 04, 2012. The reflectivity distribution at 2 km ASL is contoured by solid lines every 6 dBZ from 36 dBZ. The solid and dashed gray-colored lines indicate the coastline and the terrain heights every 400 m, respectively. The location of the vertical cross section for Fig. 9 is depicted by a solid line in panel (a).

were maintained from 2119 LST to 2132 LST with the continuous large $N(D)$ of small-sized raindrops (blue line in Fig. 13b). Furthermore, the values of D_0 below 1.7 mm were obtained as the $N(D)$ value of small raindrops, which were larger than that of large-sized raindrops (Fig. 13a).

Site W551 experienced a large increase in $N(D)$ for small-sized raindrops to > 2000 ($m^{-3}\,mm^{-1}$) during the first 10 min (red and orange lines in Fig. 12c), whereas the maximum diameter of large-sized raindrops reached 5.8 mm. Compared to the values of $N(D)$ observed at other sites on the windward side, the $N(D)$ of middle-sized raindrops at W551 was consistent (Fig. 12c), whereas D_0 larger than 2 mm was obtained between 2125 and 2130 LST (gray line in Fig. 13a). Although the $N(D)$ of small raindrops remarkably increased (Fig. 12c), the values of $N(D)$ for middle- and large-sized raindrops were nearly constant, resulting in the near-constant value of D_0 around 2 mm (Fig. 13a). Maximum $N_T \geq 2100$ was counted at W551 (gray line in Fig. 13b). After 5 min from the start of rainfall, the maximum N_T value ≥ 2000 was identified, and D_0 values slightly decreased to 1.7 mm together with an evident increase in the value of $N(D)$ for small-sized raindrops during 2125 LST–2130 LST (orange line in Fig. 12c).

4.2.2. Mountaintop

At the highest Parsivel site of the windward side, W975 (Fig. 12d), during the first 10 min (red and orange lines), the number concentration of small-, middle-, and large-sized raindrops increased to 1095, 337, and 9.2 $m^{-3}\,mm^{-1}$, respectively. After 15 min (green lines in Fig. 12d), the number concentrations of raindrops of each size gradually decreased to 323.6, 12.0, and 0 $m^{-3}\,mm^{-1}$, respectively. Large

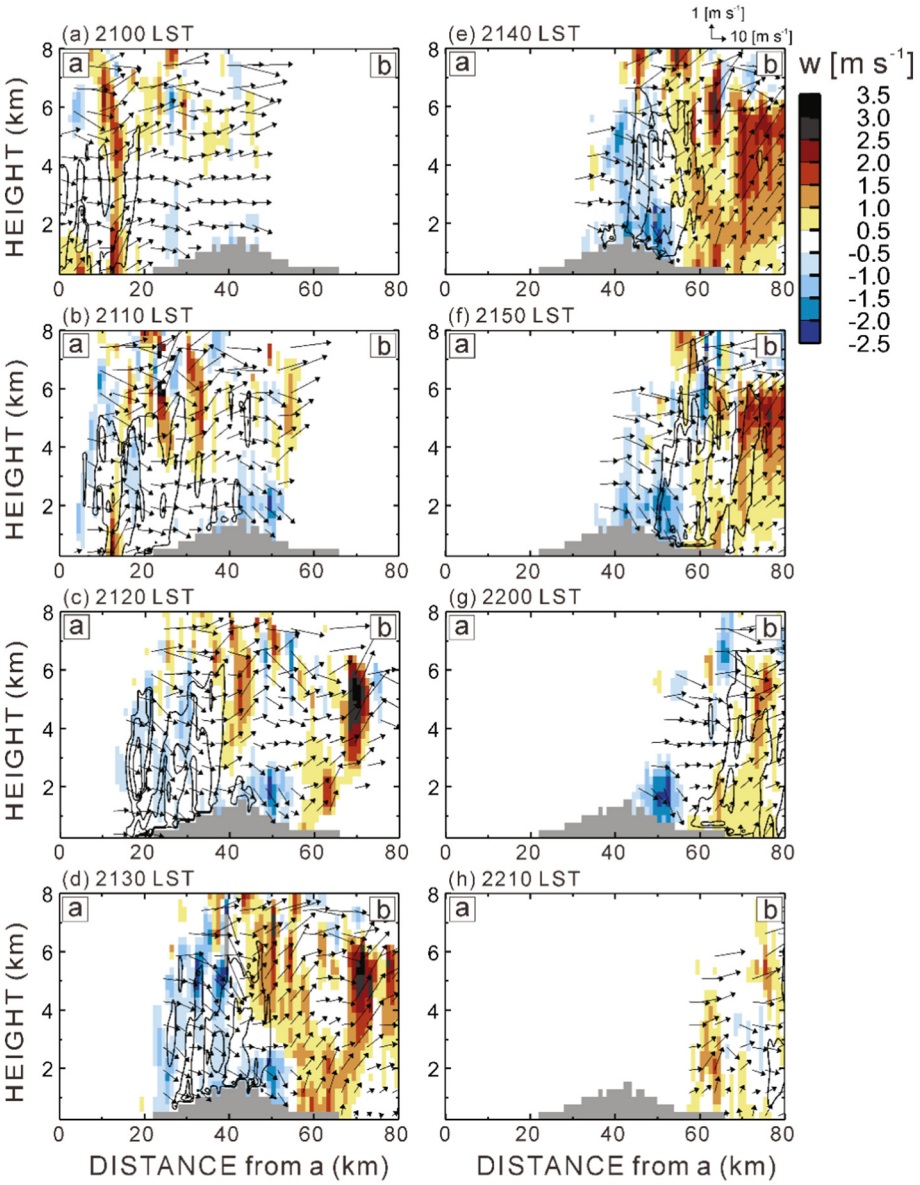

Fig. 9. The vertical distributions of the vertical wind and reflectivity along the a–b line (for the line location, see Fig. 8a) at (a) 2100 LST, (b) 2110 LST, (c) 2120 LST, (d) 2130 LST, (e) 2140 LST, (f) 2150 LST, (g) 2200 LST, and (h) 2210 LST on July 04, 2012. The reflectivity distribution is contoured every 6 dBZ from 36 dBZ. The gray-shaded area shows the topography of Jeju Island.

$D_0 \geq 2$ mm was observed at W975 after 2135 LST (black line in Fig. 13a); at W975, large N_T (~2000 m^{-3}) was counted around 2133 LST (black line in Fig. 13b). The time increasing N_T value at each site was consistent with the sharp time increase in the accumulated rain amount at W551 and W975 (Fig. 2). In addition, the increase in the small- to large-sized raindrops is consistent with the high frequency of strong reflectivity ≥30 dBZ in the R2 region (Fig. 7b).

4.2.3. Leeward side

The averaged values of $N(D)$ computed at 5-min intervals at E571, E332, and E58 on the leeward side of the mountain are displayed in Fig. 14. On the leeward side, the $N(D)$ of middle-sized raindrops were relatively lower than those on the windward side (Fig. 12); for instance 95 m^{-3} mm^{-1} at E571 (Fig. 14a), 105 m^{-3} mm^{-1} at E332 (Fig. 14b), and 77 m^{-3} mm^{-1} at E58 (Fig. 14c). Furthermore, raindrops larger than 5 mm were barely observed.

At E571, as rainfall began (red line of Fig. 14a), the $N(D)$ of small raindrops reached a relatively large value of ~745 m^{-3} mm^{-1}, and the number concentrations between 500 and 1000 m^{-3} mm^{-1} were consistently obtained during the next 20 min (yellow to green lines in Fig. 14a). After the first 10 min (orange line in Fig. 14a), raindrops larger than 3 mm were identified, whereas the maximum $N(D)$ of ~910 m^{-3} mm^{-1} for small-sized raindrops characterized the next 10 min (green line of Fig. 14a). Fig. 10 depicts the increased N_T values with the large amount of small-sized raindrops between 2135 and2140 LST (red line in Fig. 13a) as well as the D_0 value increasing from 2132 to 2138 LST (red line in Fig. 13b).

The variability of the number concentration of small raindrops at E332 (Fig. 14b) was relatively large compared to other sites on the leeward side (Fig. 14a and 14c). The maximum $N(D)$ of small raindrops reached ≥2000 m^{-3} mm^{-1}, and the raindrops grew to be > 4 mm in diameter (green line in Fig. 14b) within 25 min of rainfall. The maximum values of D_0 and N_T were 1.7 mm and > 1000, respectively, and were observed around 2203 LST (orange lines in Fig. 13a and 13b). This large concentration of small-sized raindrops is consistent with the high frequency of weak reflectivity 10–20 dBZ (Fig. 7c) from the surface to altitudes higher than 6 km ASL. Notably, during the first 30 min of rainfall (blue line in Fig. 14b), the value of $N(D)$ of small-sized

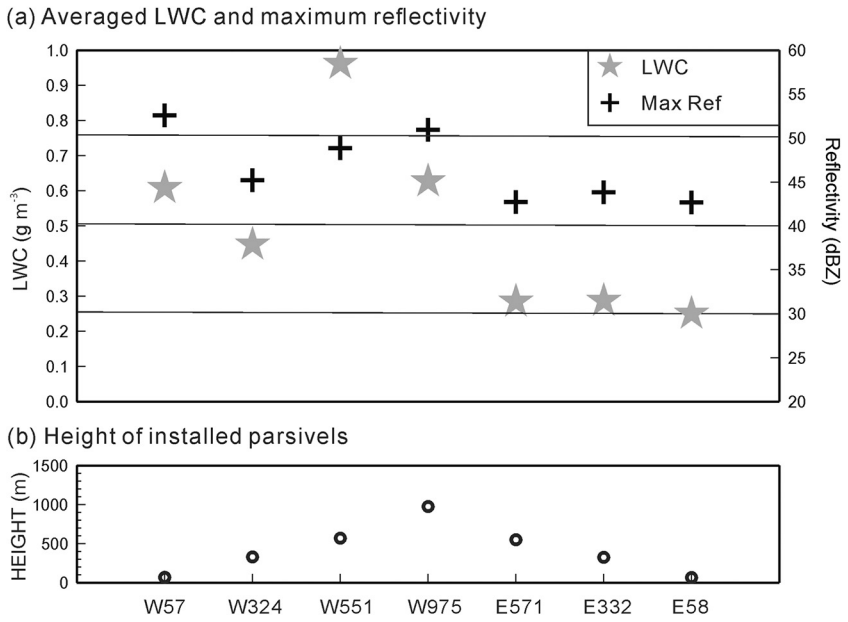

Fig. 10. (a) The averaged LWC (g m^{-3}, gray stars) and maximum reflectivity (dBZ, cross marks) during the analysis period at the 7 Parsivel sites and (b) the installed altitudes (m, open circles) of each Parsivel site.

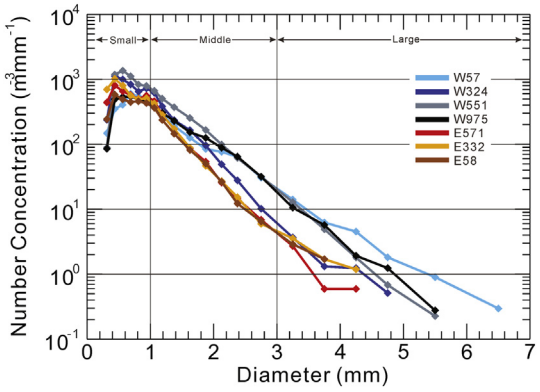

Fig. 11. Averaged number concentrations ($m^{-3}\,mm^{-1}$) of raindrops at the 7 Parsivel sites during the entire analysis period.

raindrops was consistent around 1300 $m^{-3}\,mm^{-1}$.

Raindrops larger than 4 mm were barely measured at site E58 (Fig. 14c). Raindrops larger than 3 mm were detected during the first 5 min of rainfall (orange line in Fig. 14c). Over the next 5 min, the maximum $N(D)$ (above 1000 $m^{-3}\,mm^{-1}$) of small-sized raindrops obtained at E58 (brown line in Fig. 14c) was observed with large D_0 and N_T of 1.7 mm and ~1015, respectively, at approximately 2210 LST (brown lines in Fig. 13a and 13b).

5. Discussion and conclusions

The objective of the dedicated DSD analysis using 7 Parsivel disdrometers installed along the mountain range during the special observation period from June 25 to July 15, 2012 was to investigate the microphysical characteristics of a convective precipitation system that passed over Mt. Halla (mountaintop 1950 m) of Jeju Island, South Korea, in a moist environment; the findings regarding the system that passed over Mt. Halla on July 4, 2012 are reported herein. To understand the evolution of convective precipitation and its enhancement mechanisms, we utilized data on 3D reflectivity and wind fields at high temporal (10 min) and spatial (1 km in horizontal, 0.25 km in vertical) resolutions obtained from two operational S-band Doppler radars (GSN and SSP, star marks in Fig. 1) run by the KMA.

While the eastward-moving precipitation system approached the western coastal region of Jeju Island from the sea, the convective region within the precipitation system developed both horizontally and vertically. The prevailing southwesterly winds found at low altitudes (below 2 km ASL) supplied the warm and moist air from the surface of the sea to the western coastal region (near sea-surface air temperature: 21.7 °C; sea surface temperature: 23 °C; LCL: 100 m ASL). In the moist environment of the low altitudes, the local coastal ascending airs $\geq 1\ m\,s^{-1}$ play an important role in developing the convective region. It is worth emphasizing that the number concentration, $N(D)$, of small-sized raindrops decreased, whereas the number concentration of large-sized raindrops increased, and raindrops of diameters larger than 6 mm were recorded. The developmental characteristics of the rainfall caused by the local coastal ascending air are consistent with those of Lee et al. (2014) and Yu and Jou (2005). In the study of Lee et al. (2014), the precipitation system was influenced by an updraft that occurs in the lower 1.5-km-ASL layer while passing over the northwest part of Jeju Island; as a result, a high vapor mixing ratio was obtained. Yu and Jou (2005) found that the precipitation flowed onto the coastal line developed in the lower 1-km-ASL layer owing to the convergence developed in the coastal line and thus developed moist convection. The growth of large raindrops was further accelerated by the orographically induced local ascending air at the foothill of Mt. Halla with the warm and moist marine air supplied by the low-level southwesterly wind. Our results are consistent with those of Zwiebel et al. (2016). In their study a mesoscale convective system developed over a mountain slope (top height: 700 m) and was fed at low altitudes by a supply of warm and humid air from the sea. During system development, the falling time for the small-sized raindrops increased owing to the ascending air, and this effect reinforced the growth of raindrops through coalescence. The combination of the very moist environment at low altitudes below 2 km ASL and the orographically induced local ascending air mass is crucial to activate the warm rain process, namely coalescence, condensation, and the production of a large number concentration $N(D)$ of large-sized raindrops from the western coast to the foothill of the mountain.

While the convective region continued to propagate eastward and develop on the western slope of the mountain, fed by the moist ascending airs $\geq 2\ m\,s^{-1}$, the number concentration of small and middle raindrops ($D < 3$ mm), the *LWC* (0.96 g m^{-3}), the reflectivity (48

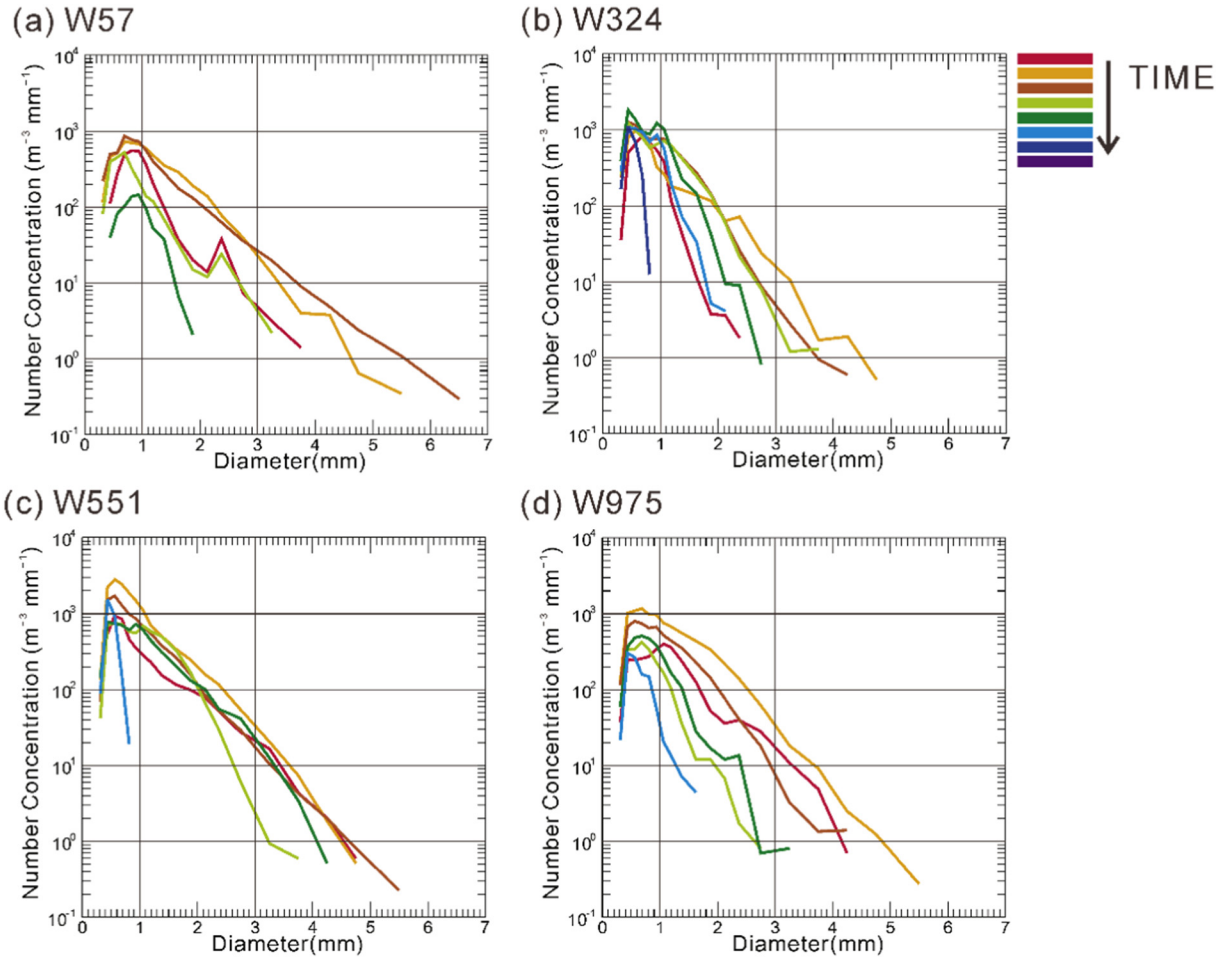

Fig. 12. The averaged number concentration ($m^{-3}\,mm^{-1}$) of raindrops every 5 min at (a) W57, (b) W324, (c) W551, and (d) W975 on the windward side of the island are displayed by the solid colored lines. The colour of the line evolves with time. For example, the DSD averaged during the first 5 min is indicated by the red-colored line. (For interpretation of the references to colour in this figure legend, the reader is referred to the web version of this article.)

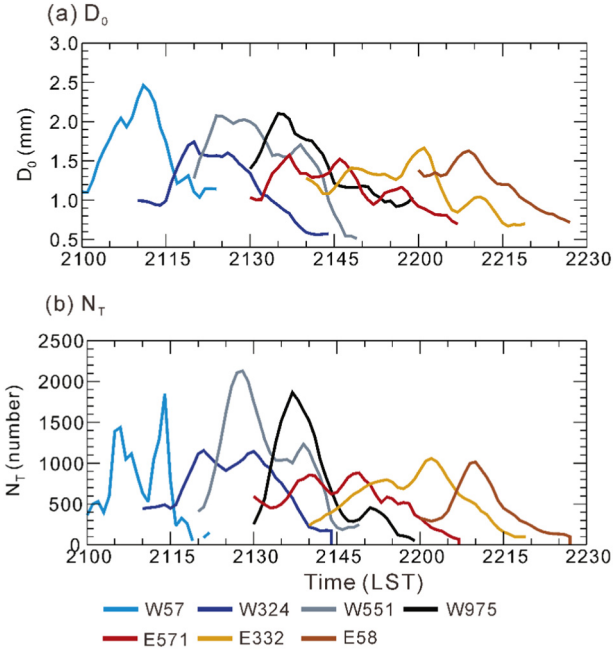

Fig. 13. Time series of the DSD parameters (a) D_0 and (b) N_T from 2100 LST to 2230 LST on July 04, 2012.

dBZ), and the accumulated rainrate (14.3 mm) increased with a high normalized frequency ≥ 60% of the stronreflectivity (30–40 dBZ) from near surface upto 6 km. Together with the advection of large-sized raindrops from the coast to the western slope, the increase of small to middle raindrops seem to contribute to increase the reflectivity. The increase of small raindrops and moisture content on the windward slope was similarly seen in previous studies (e.g., Feng and Chen Wang, 2011; Hachani et al., 2017). In Feng and Chen Wang (2011), a precipitation system passed over the windward side of the CMR of Taiwan in a moist environment with low altitudes of *LCL* (300 m ASL) and *EL* (7 km ASL), and the stratiform region within the precipitation system developed. They found an increased $N(D)$ of condensed small raindrops, a product of low-level moisture contents uptaken by the orographically induced local ascending air. They also reported that the locally ascended moisture accelerates the condensation of the vapor and cloud particles to raindrops and enhances the rainfall intensity of the stratiform region. Similarly Hachani et al. (2017) showed the orographic influences in the size and density of rain drops at different mountainous location (e.g., mountainous region with the altitude ≥ 500 m, transition zone between 300 and 500 m ASL, and hilly area with the altitude ≤ 300 m) using in-situ disdrometer observation data from 2012 to 2016. They found that the mountainous region had larger density and maximum size of raindrop than hilly area, and the coalescence and break up processes are active simultaneously over the mountainous region with large DSD variation, as similarly seen in our study. In our study, even though we studied in an *Fr* (0.2) environment, which is higher than that considered by Feng and Chen Wang (2011; $Fr = 1.4$), it

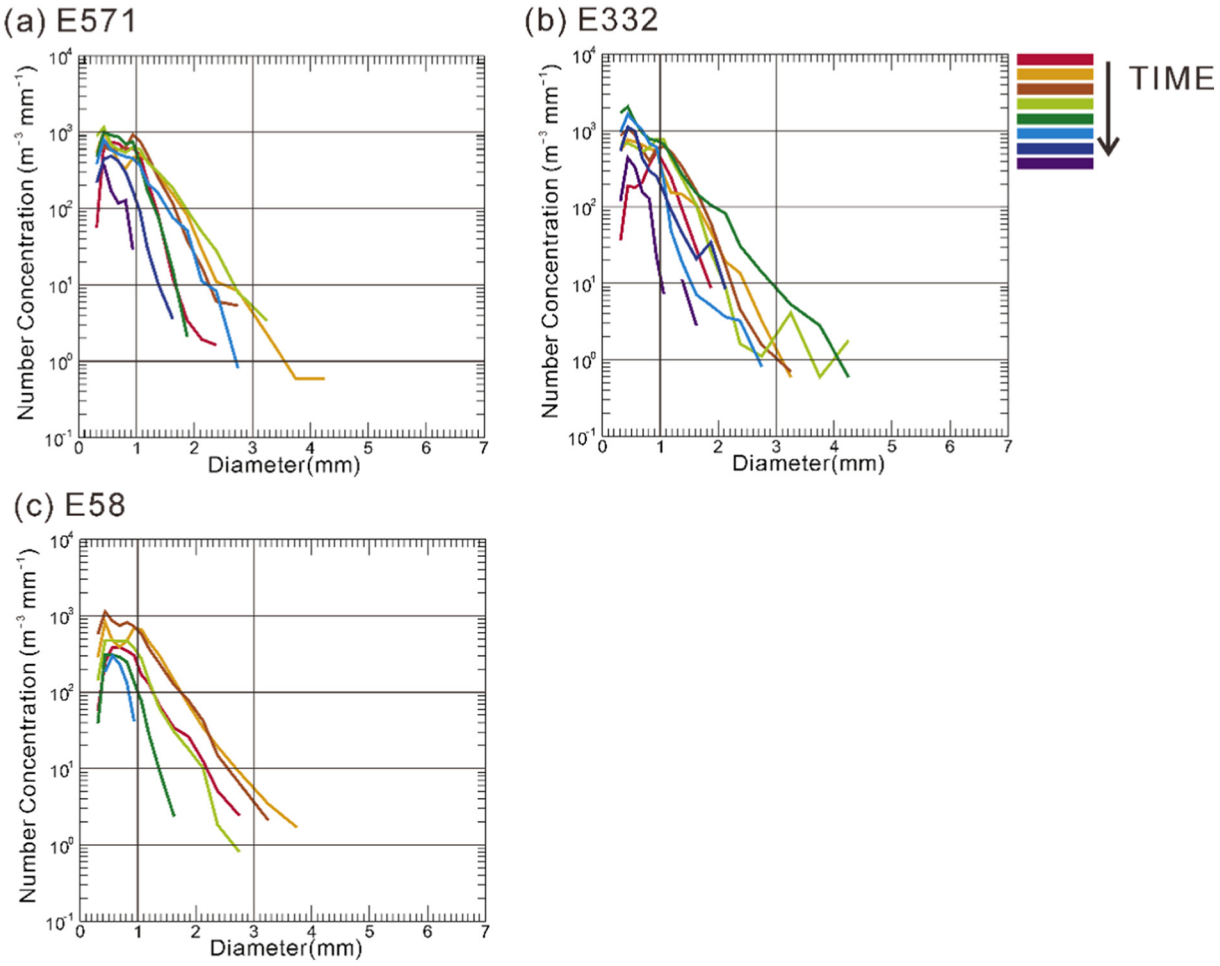

Fig. 14. Same as Fig. 13 but for the leeward side of the mountain: (a) E571, (b) E332, and (c) E58.

appears that the convective updraft (0.3 m s^{-1}) at the lowermost part of the convection region brings the low-level moisture into the convection along the gentle slope of the mountain. The supplied moisture then rapidly grows to small-sized raindrops activated by the warm rain processes of accretion, breakup, and condensation (Rosenfeld and Ulbrich, 2003) occurring in moist environments with a very low altitude of LCL (< 100 m ASL).

While the precipitation system was moving over the mountaintop, the convective region continuously developed, especially below 2 km ASL, thus highlighting the increase in the number concentration of middle and large raindrops, and maintaining a large frequency (above 50%) for strong reflectivities ≥30 dBZ below 5 km ASL. Within the convective region, descending air (1.5 m s^{-1}) intensified owing to strong precipitation. In addition, reflectivities stronger than 48 dBZ were continuously observed at altitudes of 2–4 km ASL. Ahead of the convective region, on the eastern slope of Mt. Halla, the stationary moist ascending air ≥1 m s^{-1} is the most notable feature of the system. Later, the convective region passed over the stationary ascending air region, and the increases in the $N(D)$ of small-sized raindrops and the reflectivity at altitudes lower than 2 km ASL are worth highlighting. The stationary moist ascending air at the leeward side of Mt. Halla was studied by Lee et al. (2012). They found that the relatively-weak low-level winds (Fr = 0.2) detoured the horizontal wind from the windward side of the terrain, thereby generating the local wind convergence observed on the leeward side of the mountain. The orographically induced local convergence over the leeward side delivers abundant moist and warm near sea-surface air into the convective region. In this study, with a similar environment to Lee et al. (2012) of low Fr (0.2) and large moisture (RH = 94%), we observed the maximal $N(D)$ value of small-sized raindrops on the leeward side. Also we found the frequency of both the weak and moderate reflectivities (10–30 dBZ) were strong, exceeding 70%, from the surface to altitudes above the 0 °C level. Owing to the orographically induced stationary wind convergence, the warm rain process of condensation, collection, and the breakup of falling large raindrops, maintains the precipitation intensity on the leeward side. The results of the increasing heights of reflectivity areas stronger than 33 dBZ and the development of a reflectivity area above the 0 °C level on the leeward side were also observed by Lee et al. (2014). In their study, the local moist updraft, which was distributed to 6 km (above the 0 °C level) on the leeward side of Jeju Island, could develop a convective cell with increasing graupel at heights from 3.8 to 6.0 km. This updraft could aid microphysical interactions such as conversion and the collection of cloud water, and rainwater at heights above the 0 °C level. The development of hydrometeors above the 0 °C level could be affected by stationary wind convergence on the leeward side and the effect of the mountainous terrain.

The key results of this study are summarized as follows.

(1) From the western coastal region to the mountain's foothill, the convective region within the precipitation system was developed by a combination of coastal ascending air and very warm and moist low-level marine inflow. The uptaken water vapor and cloud droplets from the sea surface into the system grew to large-sized raindrops owing to activated warm rain processes, such as coalescence and condensation, in a very warm and moist environment during the Changma season.

(2) From the upslope to the mountaintop, the low-level southwesterly winds blow along the relatively gentle upslope of Mt. Halla and they continue supplying marine moisture content to the convective region. Owing to this influx of moisture, the condensation process of small-, middle-, and large-sized drops is activated, resulting in a significant concentration of large-sized raindrops. At the mountaintop, the breakup process appears to be activated by the intensified descending air caused by falling precipitation, thereby resulting in a large concentration of small-sized raindrops.
(3) With regard to the leeward side of the mountain, ahead of the eastward-moving convective region, the orographically generated stationary ascending air region becomes significant. Owing to this ascending air and low-level marine inflow, the convective region continues to develop on the leeward side of the mountain, activating the warm rain processes of condensation and collection. This results in a large increase of small-sized raindrops.

This study revealed the DSD characteristics of several relative locations (e.g., mountainous coastal region, windward, mountaintop, and leeward side) on a single mountaintop of Jeju Island during the passage of a convective system in a warm and moist environment. We investigated the microphysical process that increases precipitation enhancement in the lower troposphere using a combination of high temporal and spatial resolution Parsivel disdrometer data (concentration and diameter of raindrops as well as water content) retrieved during an intensive field campaign and dual S-band Doppler radar data (reflectivity and wind). Based on the results of this study, an intensive field campaign using S-band polarimetric radar and video sounding is required to deepen our understanding of more detailed cloud processes at high altitudes (temperature: $\leq 0\,^{\circ}C$, ascending top height of reflectivity (≥ 33 dBZ) on the leeward side, and maximum reflectivities at 4–6 km ASL). This study focuses on the case analysis that continues with the statistical analysis of orographic precipitation using the radar and in-situ surface (disdrometer) observation data. Factors influencing precipitation development include not only orographic factors but also non-orographic factors such as wind intensity, sea surface temperature, and atmospheric stability. Therefore, much more storm case studies and statistical analyses considering non-geomorphic factors are required in the future. In addition, aircraft observations and modelling studies will be needed to understand more detailed microphysical characteristics of a convective precipitation. In future works, complementary investigations into the DSD characteristic of other MCS events under various wind regimes will be conducted to enhance our comprehension of microphysical processes occurring in precipitation systems passing over Jeju Island. Via a statistical analysis based on the various wind regimes of microphysical processes of precipitation systems such as MCS, we can expect to reveal the cause of different rainfall amount distributions based on the wind regimes on Jeju Island. Furthermore, by predicting the rainfall distribution based on statistical microphysical analyses, predicting dangerous events such as landslides, flash floods, and localized heavy rainfall is possible.

In addition, Jeju Island is close to the ocean and it appears that the development of precipitation systems is influenced by differences in CCN (cloud condensation nuclei), sea-salt, and aerosol particles developed on the ocean because of different wind speeds and wind directions at low levels. Therefore, additional analyses on the characteristics of rainfall development considering CCN, sea-salt, and aerosol particles in the future will help clarify the causes of locally developed rainfall by orographic effects.

Acknowledgments

We would like to express our appreciation to the editor and reviewers for their constructive comments. This research was supported by the Korea Meteorological Institute under Grant KMI 2018-05410.

References

Atlas, D., Srivastava, R.C., Sekhon, R.S., 1973. Doppler radar characteristics of precipitation at vertical incidence. Rev. Geophys. Space Phys. 11, 1−−35.
Cressman, G.W., 1959. An operational objective analysis system. Mon. Weather Rev. 87, 367–374.
Feng, Y.C., Chen Wang, T.C., 2011. Precipitation characteristics of an autumn torrential rainfall event in northern Taiwan as determined from dual-polarization radar data. J. Meteorol. Soc. Jpn. 89, 133–150.
Gamache, J.F., Houze Jr., R.A., 1982. Mesoscale air motions associated with a tropical squall line. Mon. Weather Rev. 110, 118–135.
Hachani, S., Boudevillain, B., Delrieu, G., Bargaoui, Z., 2017. Drop size distribution climatology in Cévennes-Vivarais region, France. Atmosphere 8, 233. https://doi.org/10.3390/atmos8120233.
Jaffrain, J., Berne, A., 2010. Experimental quantification of the sampling uncertainty associated with measurements from Parsivel disdrometers. J. Hydrometeorol. 12, 352–370.
Jiang, Q., 2003. Moist dynamics and orographic precipitation. Tellus 55A, 301–316.
Kruger, A., Krajewski, W.F., 2002. Two-dimensional video disdrometer: A description. J. Atmos. Ocean. Technol. 19, 602–617.
Lee, K.O., Shimizu, S., Maki, M., You, C.H., Uyeda, H., Lee, D.I., 2010. Enhancement mechanism of the 30 June 2006 precipitation system observed over the northwestern slope of Mt. Halla, Jeju Island, Korea. Atmos. Res. 97, 343–358.
Lee, K.O., Uyeda, H., Shimizu, S., Lee, D.I., 2012. Dual-doppler radar analysis of the enhancement of a precipitation system on the northern side of Mt. Halla, Jeju Island, Korea on 6 July 2007. Atmos. Res. 118, 133–152.
Lee, K.O., Uyeda, H., Lee, D.I., 2014. Microphysical structures associated with enhancement of convective cells over Mt. Halla, Jeju Island, Korea on 6 July 2007. Atmos. Res. 135–136, 76–90.
Lin, Y.L., Chiao, S., Wang, T.A., Kaplan, M.L., Weglarz, R.P., 2001. Some common ingredients for heavy orographic rainfall. Weather Forecast. 16, 633–659.
Liou, Y.C., Chang, Y.J., 2009. A variational multiple-doppler radar three-dimensional wind synthesis method and its impacts on thermodynamic retrieval. Mon. Weather Rev. 137, 3992–4010.
Löffler-Mang, M., Joss, J., 2000. An optical disdrometer for measuring size and velocity of hydrometeors. J. Atmos. Ocean. Technol. 17 (2), 130–139.
Massmann, A.K., Minder, J.R., Garreaud, R.D., Kingsmill, D.E., Valenzuela, R.A., Montecinos, A., Fults, S.L., Snider, J.R., 2017. The Chilean coastal orographic precipitation experiment: observing the influence of microphysical rain regimes on coastal orographic precipitation. J. Hydrometeorol. 18, 2723–2743.
Riemann-Campe, K., Fraedrich, K., Lunkeit, F., 2009. Global climatology of convective available potential energy (CAPE) and convective inhibition (CIN) in ERA-40 reanalysis. Atmos. Res. 93, 534–545.
Rosenfeld, D., Ulbrich, C.W., 2003. Cloud microphysical properties, processes, and rainfall estimation opportunities. Meteorol. Monogr. 30, 237–258.
Ulbrich, C.W., 1983. Natural variations in the analytical from of the raindrop size distribution. J. Climate Appl. Meteorol. 22, 1764–1775.
Vivekanandan, J., Zhang, G., Brandes, E., 2003. Polarimetric radar estimators based on a constrained gamma drop size distribution model. Amer. Meteorol. 43, 217–230.
Yoshizaki, M., Kato, T., Tanaka, Y., Takayama, H., Shoji, Y., Seko, H., 2000. Analytical and numerical study of the 26 June 1998 orographic rainband observed in western Kyushu, Japan. J. Meteorol. Soc. Jpn. 78, 835–856.
Yu, C.K., Jou, B.J.-D., 2005. Radar observations of the diurnally forced offshore convective lines along the southeastern coast of Taiwan. Mon. Weather Rev. 133, 1613–1636.
Yuter, S.E., Houze Jr., R.A., 1995. Three-dimensional kinematic and microphysical evolution of Florida Cumulonimbus. Part II: Frequency distributions of vertical velocity, reflectivity, and differential reflectivity. Mon. Weather Rev. 123, 1941–1963.
Zwiebel, J., Van Baelen, J., Anquetin, S., Pointin, Y., Boudevillain, B., 2016. Impacts of orography and rain intensity on rainfall structure. The case of the HyMeX IOP7a event. Q. J. R. Meteorol. Soc. 142, 310–319.